# A simulation study of the time measurement accuracy for the SPACAL type ECAL Module for LHCb Upgrade phase 2

LHCb-PUB-2020-004
26/05/2020



**Public Note**

Issue: 1
Revision: 0

Reference: LHCb-PUB-2020-004
Created: February 15, 2020
Last modified: June 12, 2020

**Prepared by:** Y. Talochka[a], E. Auffray[b], A. Golutvin[cd], Yu. Guz[e], D. Kazlou[a], M. Korjik[f], L. Martinazzoli[g], V. Mechinsky[b], M. Pizzichemi[g], A. Schopper[g], E. Shmanin[c]

[a]Research Institute for Nuclear Problems of Belarusian State University (INP BSU), Minsk, Belarus

[b]Crystal Clear Collaboration, CERN, Geneva, Switzerland

[c]National University of Science and Technology (MISIS), Moscow, Russia

[d]Imperial College London, London, United Kingdom

[e]National Research Centre "Kurchatov Institute" – IHEP, Protvino, Russia

[f]National Research Centre "Kurchatov Institute", Moscow, Russia

[g]CERN, Geneva, Switzerland

# Abstract

The Spaghetti type Calorimeter (SPACAL) with fibers parallel to the beam direction is considered as an option for the inner part of the future LHCb Electromagnetic Calorimeter (ECAL) for the Upgrade Phase 2. In this work we have developed a method of fast simulation of optical photon transport for this type of calorimeters and a method of simulation of the photodetector response. The studies of intrinsic precision of time measurement with such calorimeters have been performed for the electron and photon beams with energies of 1, 2, 4, 5 and 10 GeV.

# Document Status Sheet

| **1. Document Title: A simulation study of the time measurement accuracy for the SPACAL type ECAL Module for LHCb Upgrade phase 2** | | | |
|---|---|---|---|
| **2. Document Reference Number: LHCb-PUB-2020-004** | | | |
| **3. Issue** | **4. Revision** | **5. Date** | **6. Reason for change** |
| Draft | 0.0 | February 15, 2020 | Draft version |
| Draft | 0.1 | April 15, 2020 | Draft version, corrected |
| Draft | 1.0 | May 17, 2020 | Version 1.0, submitted |
| Version | 1.1 | June 12, 2020 | Version 1.1, comments are implemented, more material added |

# Contents

# List of Figures



# List of Tables

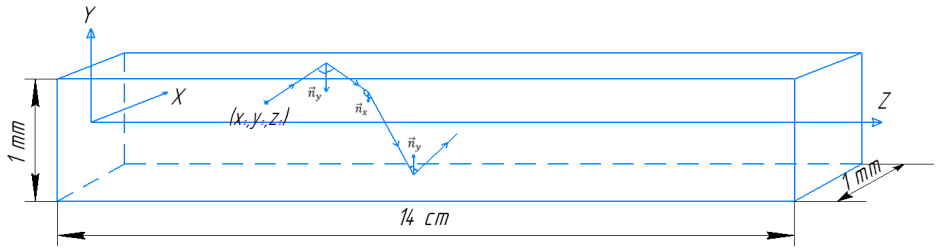


**Figure 1** Illustration of passage of a scintillation photon through a fiber.

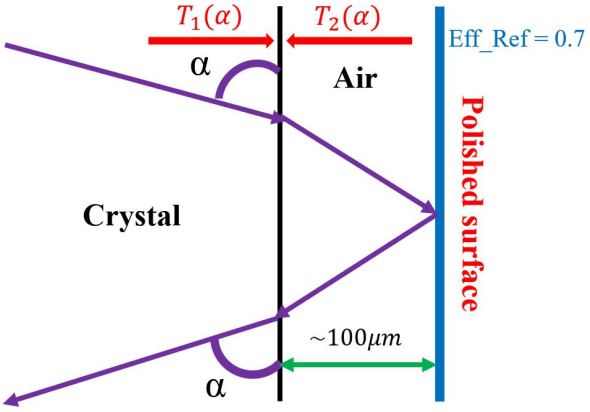


**Figure 2** Light path at the end of fiber with mirror.

# 1 Introduction

Spaghetti type calorimeter (SPACAL) with fibers parallel to the beam direction is being considered for the inner part of the future Electromagnetic Calorimeter (ECAL) for the LHCb Upgrade 2 [1]. Because of the significant increase of the radiation dose at the LHCb Upgrade 2, a radiation hard scintillating material should be used, such as YAG:Ce or GAGG:Ce crystals [2, 3].

In this note we study the intrinsic time resolution for the SPACAL calorimeter module which is split longitudinally into two parts, 4 and 10 cm long. For the sake of comparison, the timing performance of a module filled with continuous 14 cm long fibers was also studied. More details on the detector configurations will be given in Chapter 2.

In general, the simulation of timing properties of a sampling scintillation calorimeter proceeds in three stages: simulation of energy depositions in a shower, creation of optical photons and their transportation to a photodetector.

The method presented in this note uses detailed simulation of electromagnetic showers with GEANT4 [4]. For the creation of optical photons according to energy depositions in the scintillation media it also uses procedures from GEANT4.

The procedures for the photon transport are also available in GEANT4. They perform very accurate step-by-step propagation of photons taking into account all optical effects. However, this is very CPU time consuming.

Another software package providing high quality procedures for optical photon transport is SLitrani [5]. Its operation is also very CPU time consuming.

In order to speed up the calculations, an analytical approach to the transport of optical photons has been developed. This approach is especially efficient in case of long thin scintillation elements (fibers) of SPACAL: the detailed procedure of propagation of photons towards the photo detector, including many tens of acts of total internal reflection, can be replaced by a single analytical expression. It allows to speed up the calculations, with respect to the full straightforward GEANT4 simulation, by two orders of magnitude.

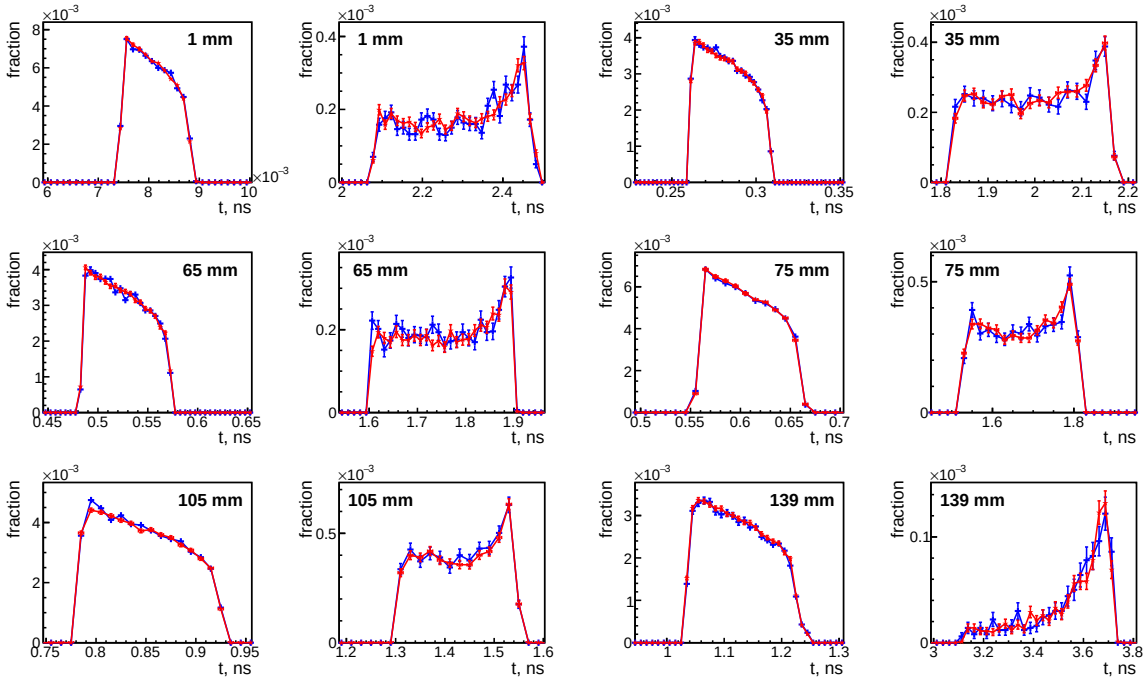


**Figure 3** Distributions of the time of transport for optical photons to the end of a 140 mm fiber. The emission point is located at distances of 1, 35, 65, 75, 105 and 139 mm from the fiber end, as indicated at the plots. The distributions obtained with full optical photon tracing of GEANT4 are shown in blue, while those obtained using the proposed method are shown in red. Two plots are given for each position, one for the photons directly arrived to the fiber end and the other one for the photons emitted into the opposite direction and arrived to the fiber end after being reflected from the other end. The plots are normalized to the total number of generated photons.

We should mention here that the method described below was built in the assumption of perfect polishing of the crystal scintillating elements. Although in reality some little roughness is present in the lateral and end surfaces, our approach can be used to estimate, at first approximation, the expected time resolution and study its dependence on various parameters of the detector. The work is ongoing on the extension of the method onto the case of finite roughness of surfaces, the results will be described in subsequent notes.

# 2 The optical photon propagation method

In this section we describe the method of calculating the time of transport and absorption probability of a scintillation photon through a fiber. This is done in the approximation of total internal reflection: we are considering only photons which were emitted at angles of total internal reflection at the fiber sides. This assumption makes sense, because in a long fiber made of a scintillation material having luminescent centers ($Ce^{3+}$ in our case) with a small Stokes shift only those photons can reach the fiber end and photodetector which were emitted at angles of total internal reflection. Indeed, the photons emitted at larger angles and going outside the fiber through its edges, are then reflected from the surface of the absorber. If the reflectivity of the absorber surface is low, after several reflections these photons get lost.

Of course, we can imagine that the surface of the absorber has a high reflection coefficient, which can be 90% or even 95% for the wavelength range of the scintillation photons. The photons going outside the fiber are emitted at large angles, and experience many reflections. The probability for such photon to reach the fiber end will essentially depend on the position of the emission point, which will deteriorate the uniformity of the light collection, and in the end the calorimeter performance. In the following we will assume that the reflection coefficient of the surface of the absorber is made low, and will consider only the photons emitted at the angles of total internal reflection.

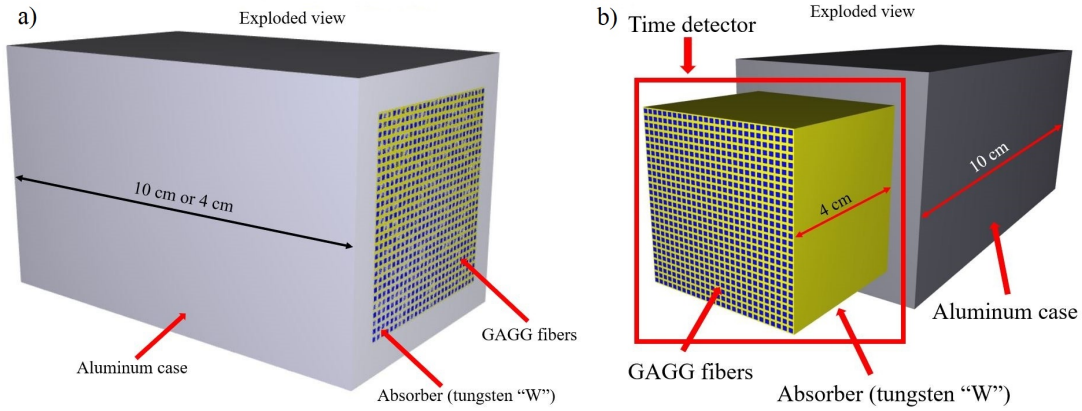


**Figure 4** The layout of the SPACAL prototypes.

The sketch of photon propagation through the fiber is shown in Figure 1.

Due to the homogeneity of the refractive index along the $Z$-axis, the time of transport of a photon can be calculated as follows:

$$\Delta t = \frac{(n_{cr} + E\frac{dn_{cr}}{dE})\,|\Theta(\cos\theta)L - z_0|}{c\,|\cos\theta|}, \tag{1}$$

where $L$ is the length of the fiber, $E$ is the photon energy, $n_{cr}$ is the refraction index of the scintillating crystal, $z_0$ is the $Z$-coordinate of the emission point, $\theta$ is the angle between the wave vector of the photon and the $Z$-axis, $\Theta(x)$ is the step function.

The equation (1) does not contain dependence on $x_0$ and $y_0$ coordinates of the emission point. This is a consequence of the fact that, during the reflection of the photons on the side surfaces, the absolute value of the projection of the photons wave vectors onto the normal to the reflecting surface is conserved.

The condition for total internal reflection [6] of scintillation photons from the side surface is:

$$|\cos\alpha| < \sqrt{1 - \frac{n^2}{n_{cr}^2}}, \quad |\cos\beta| < \sqrt{1 - \frac{n^2}{n_{cr}^2}}, \tag{2}$$

where $\alpha$ and $\beta$ are the angles between the photon wave vector and the $x$ and $y$ axes, respectively, $n_{cr}$ and $n$ are the refractive indexes of the scintillation crystal and the surrounding medium (air).

It is also necessary to take into account the case when a photon is emitted near the photodetector window and the angle between the photon direction and the normal to the side surface is less than the critical angle, but the photon does not experience reflections from the side surface, because it goes straight to the end. In this case, the following conditions must be fulfilled:

$$X_{min} \le x_0 + \frac{\cos\alpha}{\cos\theta}(L\Theta(\cos\theta) - z_0) \le X_{max}, \tag{3}$$

$$Y_{min} \le y_0 + \frac{\cos\beta}{\cos\theta}(L\Theta(\cos\theta) - z_0) \le Y_{max}, \tag{4}$$

where $X_{min}$, $X_{max}$ and $Y_{min}$, $Y_{max}$ are the boundary coordinates of the side surface of the fiber. Also, this method takes into account the probability of absorption of the photon $P_{ab}$ along its trajectory [7]:

$$P_{ab} = 1 - \exp(-\frac{|L\Theta(\cos\theta) - z_0|}{l\,|\cos\theta|}), \tag{5}$$

where $l$ is the absorption length.

Normally, the scintillator crystal and the photodetector window do not have immediate optical contact: there is a thin gap between them, which is in our study filled with air.

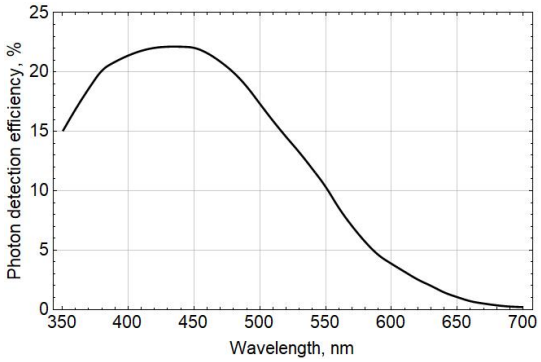


**Figure 5** The typical PMT quantum efficiency curve.

The transmission coefficient through the system crystal - air gap - photodetector window is given by the following expression:

$$T(n_{cr}, n_{opt}, n_{win}, \theta) = \frac{1}{2}\sum_{i=1}^{2}(1 - R_i(n_{cr}, n_{opt}, \theta))(1 - R_i(n_{opt}, n_{win}, \arcsin(\frac{n_{cr}}{n_{opt}}\sin\theta)))\times$$
$$(1 - R_i(n_{opt}, n_{win}, \arcsin(\frac{n_{cr}}{n_{opt}}\sin\theta))R_i(n_{opt}, n_{cr}, \arcsin(\frac{n_{cr}}{n_{opt}}\sin\theta)))^{-1}, \quad (6)$$

where $n_{opt}$ and $n_{win}$ are the refractive indexes of the air gap and the photodetector window, $R_i(n_1, n_2, \theta)$ is the reflection coefficient for $s$- and $p$- polarizations, which is calculated with Fresnel formulas [6]:

$$R_i(n_1, n_2, \theta) = \begin{cases} (\frac{\sin(\theta - \arcsin(\frac{n_1}{n_2}\sin(\theta)))}{\sin(\theta + \arcsin(\frac{n_1}{n_2}\sin(\theta)))})^2, i = 1; \\ (\frac{\tan(\theta - \arcsin(\frac{n_1}{n_2}\sin(\theta)))}{\tan(\theta + \arcsin(\frac{n_1}{n_2}\sin(\theta)))})^2, i = 2. \end{cases} \quad (7)$$

If $\frac{\pi}{2} \leq \theta \leq \pi$, we should replace $\theta \to \theta - \frac{\pi}{2}$ in (6) and (7). Also, we must take into account that the angle of incidence of the beam $\theta$, the angle of refraction in the air gap $\gamma$ and the angle $\omega$ of refraction in the material of the photodetector window must satisfy the Snell's law.

In the longitudinally split detector (see Section 3) the sections are separated by a thin double-sided mirror. The fibers are attached to it via a thin air gap (Figure 2). The calculation of the probabilities of reflection from the crystal-air interface or passing through it is calculated with the Fresnel formulas (7). The probability of reflection from the mirror in this case does not take into account the wavelength dependence.

The time of transport of a photon $\Delta t_n$ corresponding to n reflections is calculated according to (8):

$$\begin{cases} \Delta t_0 = \frac{(n_{cr} + E\frac{dn_{cr}}{dE})|z - z_0|}{c|\cos\theta|}, \\ \Delta t_1 = \Delta t_0 + \frac{(n_{cr} + E\frac{dn_{cr}}{dE})L}{c|\cos\theta|}, \\ \quad \cdots\cdots \end{cases} \quad (8)$$

Figure 3 represents the results of modeling the transport of optical photons with wavelength 520 nm, emitted by an isotropic source with coordinates $(0, 0, 1)$, $(0, 0, 35)$, $(0, 0, 65)$, $(0, 0, 75)$, $(0, 0, 105)$ and $(0, 0, 139)$ mm in the fiber (Figure 2), to the photodetector windows, which are located at the ends, using the proposed method and the full optical photon tracing of GEANT4. As can be seen from Figure 3, the simulation results are in good agreement.

# 3 SPACAL simulation

## 3.1 Layout of modules under study

The configurations of the calorimeter modules considered in this note are shown in Figure 4. A sketch of a single SPACAL section is shown in Figure 4a; the full module, consisting of the 4 and 10 cm long sections, is presented in Figure 4b.

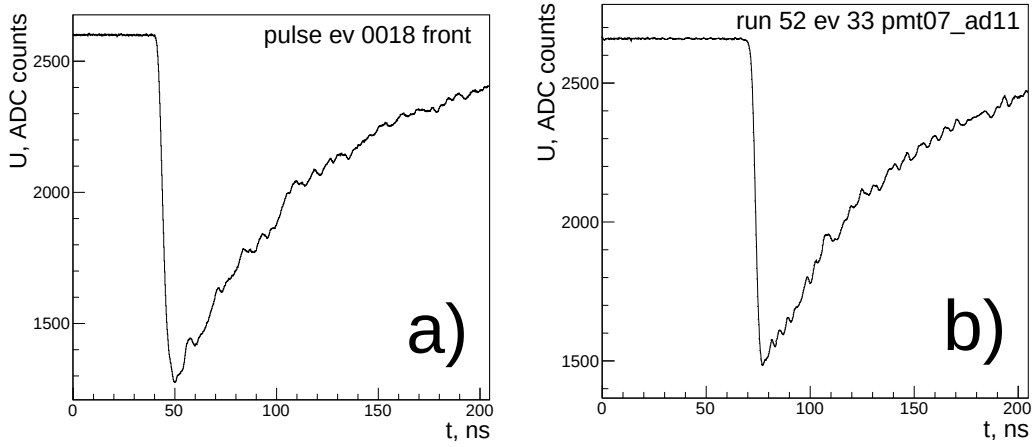


**Figure 6** The pulse shapes at the front section of the split SPACAL detector at 4 GeV electron beam: **a** simulated; **b** obtained at test beam.

Each SPACAL section consists of an absorber matrix with $27 \times 27$ square holes of $1.2 \times 1.2$ mm$^2$ cross section and 1.7 mm pitch. Each hole hosts a crystal scintillating fiber with $1 \times 1$ mm$^2$ cross section.

The two sections of the full SPACAL module are connected together and separated by a thin reflecting wall (50 $\mu$m aluminum). The light readout is performed for each module separately.

We have studied also a single 14 cm long module with continuous fibers and with light readout at both ends. Its layout is identical to that of a single SPACAL section, except for the length (14 cm).

## 3.2 Scintillating crystals

The Gadolinium-Aluminum-Gallium garnet (GAGG) doped with Cerium is used as a scintillating material for fibers.

The shape of the scintillating pulse was modeled as a sum of several components, each having its own rise and decay time:

$$f(t,t_0) = \sum_{i=1}^{n} A_i \frac{e^{-\frac{t-t_0}{\tau_{d_i}}} - e^{-\frac{t-t_0}{\tau_{r_i}}}}{\tau_{d_i} - \tau_{r_i}} \Theta(t-t_0), \tag{9}$$

where $t_0$ is the moment of ionization, $t$ is the moment of photon emission in the crystal, $\Theta(t-t_0)$ is a step function, $n$ is the number of independent scintillation components, $A_i$ is the intensity of the i-th component. $\tau_{r_i}$ and $\tau_{d_i}$ are its rise and decay time,respectively.

Table 1 and figures 14 - 16 (Appendix 8) show the optical and scintillation properties of the GAGG crystal, which are used in the simulation. These parameters are results of measurements made by authors; the details will be described in a dedicated note.

Apart from scintillation mechanism, the optical photons are produced in the crystal fibers by Čerenkov radiation. The Čerenkov photons were generated by GEANT4 with default settings, and propagated with the proposed method.

## 3.3 Incident beam

The simulation was performed for electrons and photons of energies 1, 2, 4, 5 and 10 GeV. The beam coordinates were uniformly distributed in the $(xy)$ plane within a 10 mm large square.

The direction of the beam had a tilt of 3° in each of the $(xz)$ and $(yz)$ planes. This beam direction was used for all the simulation runs discussed below. The $(x, y)$ coordinates of the tilted beam for the main detector configuration (Figure 4b) were centered at $(x = 0, y = 0)$ at the $z$ coordinate of the gap between the two sections. For the runs with the single module with continuous fibers (Figure 4a), the beam was centered at $(x = 0, y = 0)$ at $z$=4 cm from the front face.

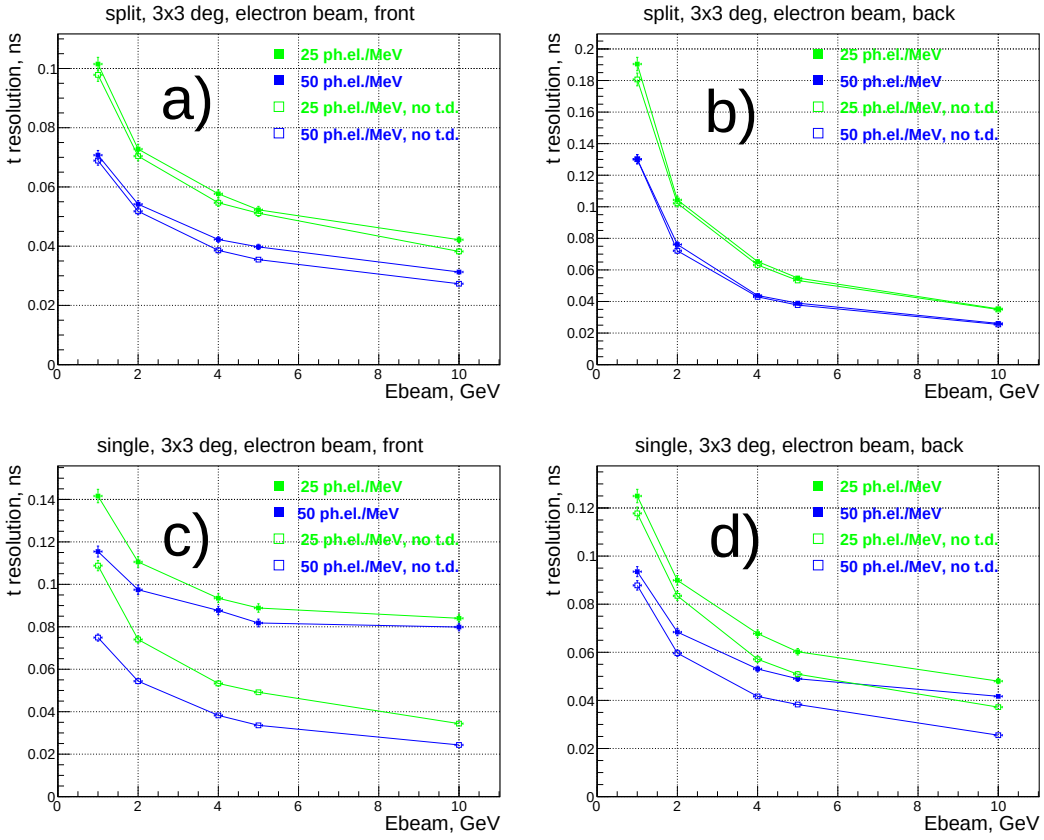


**Figure 7** The values of time resolution for the front and back photodetectors of the split SPACAL module (**a**, **b**) and for the single 14 cm long SPACAL module with continuous fibers (**c**, **d**), as a function of the incident electron energy. The beam was tilted by 3° in both $(zx)$ and $(zy)$ planes. The photoelectron yields were 25 and 50 per MeV. The graphs labeled "no t.d." correspond to the time resolution obtained without taking into account shower development and photon transport, see text.

## 3.4 Output file structure

Each optical photon reaching the photodetector was recorded into the output ROOT tree. The following information was stored:

- Event and photon serial number;
- Photon energy (wavelength);
- Origin of the photon (scintillation or Cerenkov radiation);
- The $(x, y, z)$ coordinates of the photon emission point;
- The direction of the photon;
- Time of the photon emission. The time origin is the moment of incident electron crossing the detector front face. The scintillation kinetics is not taken into account at this stage, the moment of photon emission is the moment of the energy deposition;
- Time of the photon arrival to the photodetector, and the photodetector ID (front or back).

This information can be used as a starting point for the simulation of the detector response, which is performed at the analysis stage. Namely, at the analysis stage one can vary:

- The scintillation kinetics, which is, for the same scintillator (GAGG), significantly depends on the co-doping;

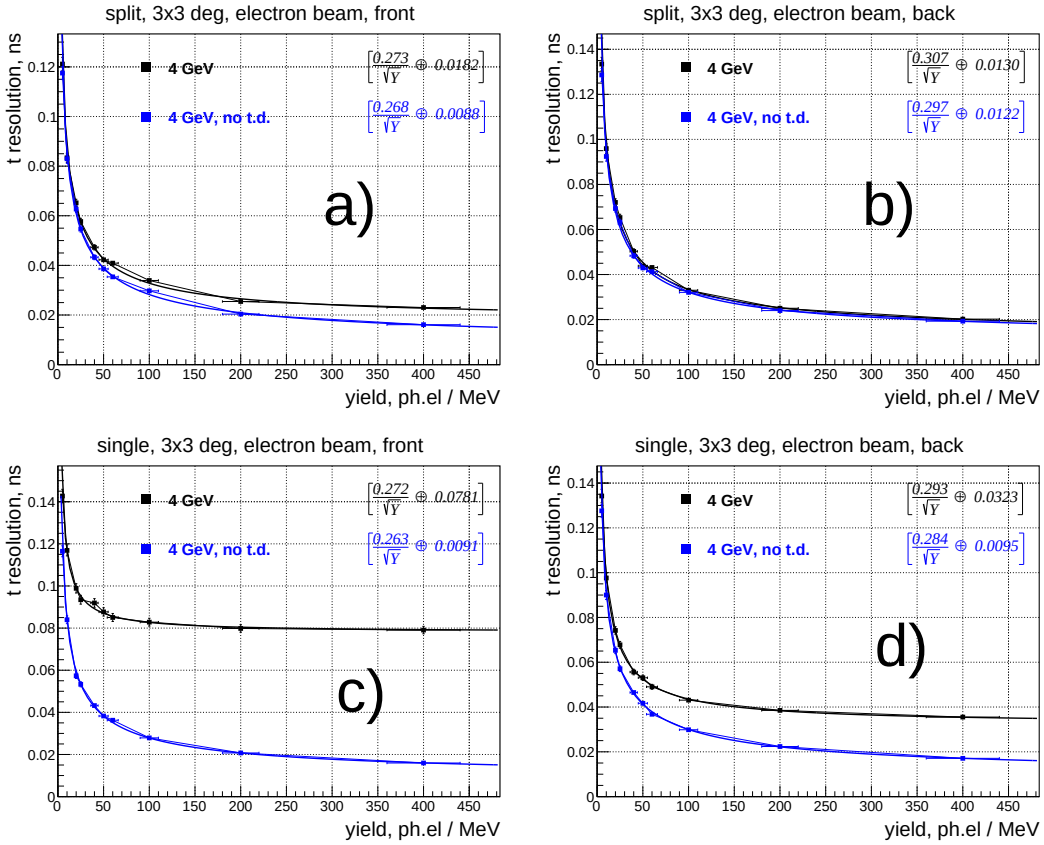


**Figure 8** The values of time resolution for the front and back photodetectors of the split SPACAL module (**a**, **b**) and of the single 14 cm long SPACAL module with continuous fibers (**c**, **d**), as a function of the photoelectron yield. The electron beam energy was 4 GeV. The graphs labeled "no t.d." correspond to the time resolution obtained without taking into account shower development and photon transport, see text.

- The photon detection efficiency of the photodetector;
- The single photoelectron pulse shape, amplitude and transit time of the photodetector;
- Parameters of signal transmission lines (e.g., cables) and analog filters can be easily included if necessary.

This gives necessary flexibility for the optimization of, e.g., parameters of electronics, which can be performed on the basis of one output file, without the need to redo the GEANT4 simulation for every change of parameters.

# 4 Detector response simulation

The properties of photodetector and electronics are applied at the analysis stage.

In our model we are assuming a standard chain consisting of a PMT connected to the crystal fiber ends through a small air gap, and a 5 GS/s waveform digitizer.

Each optical photon produces a photoelectron with a probability determined by the photon detection efficiency curve of the photodetector. In response to each photoelectron, a waveform is generated, with shape, amplitude and delay determined by crystal scintillation kinetics and properties of the photodetector. [a] The output signal is a sum of such single-electron waveforms.

[a] For Čerenkov photons, the delay determined by scintillation kinetics was not applied. The fraction of Čerenkov photons was found to be 0.02%. The effect of these photons on time measurements was studied; no statistically significant effect was observed at omission of these photons.

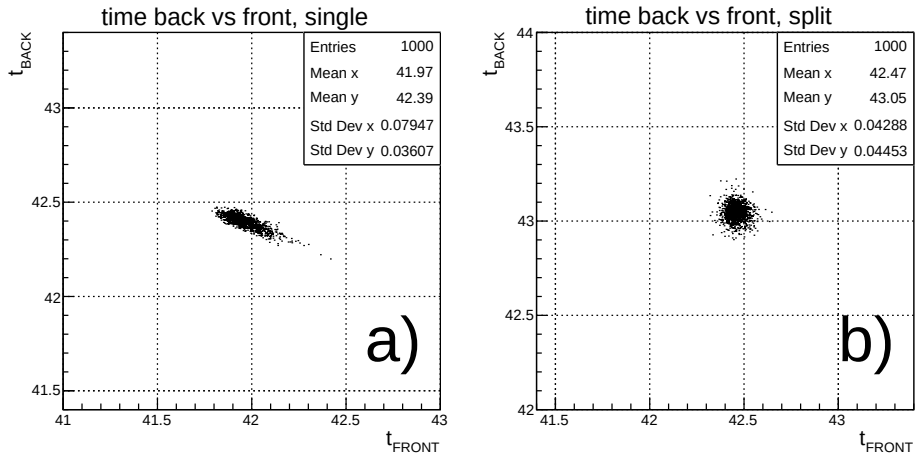


**Figure 9** Correlation of time measurements for the front and back photodetectors of the SPACAL module with continuous fibers (a) and split SPACAL module (b).

We used typical characteristics of a high quality head-on, linear-focused PMT. Its response was parameterized as follows:

- Single electron pulse shape:
$$u(t) = \frac{RGe}{\tau^3} t^2 e^{-\frac{t}{\tau}}. \tag{10}$$
Here $R$ is the input impedance of the electronics (50 Ohm), $G$ is the PMT gain, $e$ is the electron charge, $\tau$ is the time constant (typically 1 ns).

- Single electron pulse amplitude distribution: this is a Gamma-distribution
$$S(A;\alpha,\beta) = \frac{\beta/\alpha}{\Gamma(\beta)} (\frac{\beta}{\alpha} A)^{\beta-1} \exp{(-\frac{\beta}{\alpha} A)}. \tag{11}$$
Here $A$ is the pulse amplitude; $\alpha$ and $\beta$ are the scale and shape parameters, respectively. The mean of this distribution $< A >= \alpha$. The shape parameter $\beta$ was taken to be $6.0$.

- The interval of time between creation of a photoelectron and start of the anode pulse is called transit time. The transit time depends on a coordinate at the photodetector window. Assuming that each photon gets into a random point at the photodetector, we generate the transit time as a sum of constant delay (40 ns) and a Gaussian with spread of 1 ns.

- For the photon detection efficiency, we have taken that for typical bialkali photocathodes (Figure 5), which varies, in the spectral range of interest, from ∼15% at 520 nm down to 1% at 650 nm.

- On top of it, we can adjust the photon detection efficiency, in order to account for possible light losses, by skipping a certain part of photons at the analysis stage. Moreover, in order to study the performance in hypothetical cases of elevated photoelectron yield, we can use each optical photon several times, each time generating new photoelectron creation time according to scintillation kinetics and photodetector properties.

The time reconstruction algorithm is an "offline constant fraction discriminator (CFD)", i.e. we determine the moment of time when the waveform crosses the level of a certain fraction of the signal maximum. For this study, the value of 20% was chosen, as it is close to the optimum for all beam energies.

It is important to mention here that we considered the digitizer to be "ideal" and did not take into account any imperfections of a real device, like non-equidistant sampling intervals or cross-talk between channels. As an example, some performance features of popular digitizer DT5742 produced by CAEN are studied in [8].

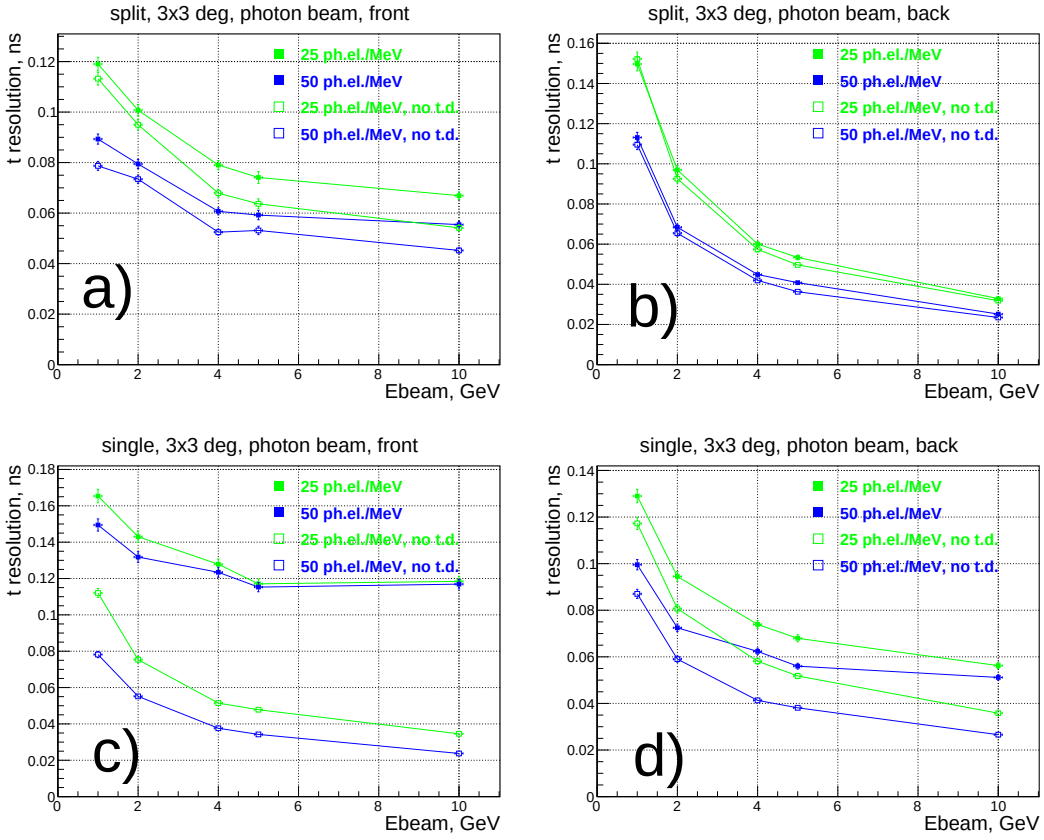


**Figure 10** The values of time resolution for the front and back photodetectors of the split SPACAL module (**a**, **b**) and for the SPACAL module with continuous fibers (**c**, **d**), as a function of the incident photon energy. The beam was tilted by 3° in both $(zx)$ and $(zy)$ planes. The photoelectron yields were 25 and 50 per MeV. The graphs labeled "no t.d." correspond to the time resolution obtained without taking into account shower development and photon transport, see text.

# 5 Results and discussion

The typical pulse shapes from this simulation study and from the beam test are shown in Figure 6. One can see that the pulse shape is reproduced satisfactorily.

## 5.1 Electron beam

The simulated photoelectron yield for the split SPACAL module turned out to be 49.5 photoelectrons per MeV of energy deposition in the detector.

The simulation was therefore performed for two values of photoelectron yields, 50 and 25 per MeV. For the real detector, the former can correspond to the case of direct mounting of PMTs onto the SPACAL module (via a thin air gap), while the latter may be caused either by light losses which occur in case of using a light guide between the SPACAL module and PMT, or by using scintillation material with lower light yield.

We also studied the SPACAL performance in a wide range of photoelectron yields, from 5 to 400 photoelectrons per MeV. The low values may correspond to accidental additional light losses, while the high values may be obtained when improving the light collection scheme: for instance, using a photodetector with better quantum efficiency, or arranging a direct optical contact of the scintillating fibers to the photodetector entrance window, without the air gap.

Figure 7 shows the values of time resolution for the front and back photodetectors of the split (a, b) and continuous (c,d) SPACAL modules, as a function of the incident electron energy, for the photoelectron yield of 25 and 50 per MeV.

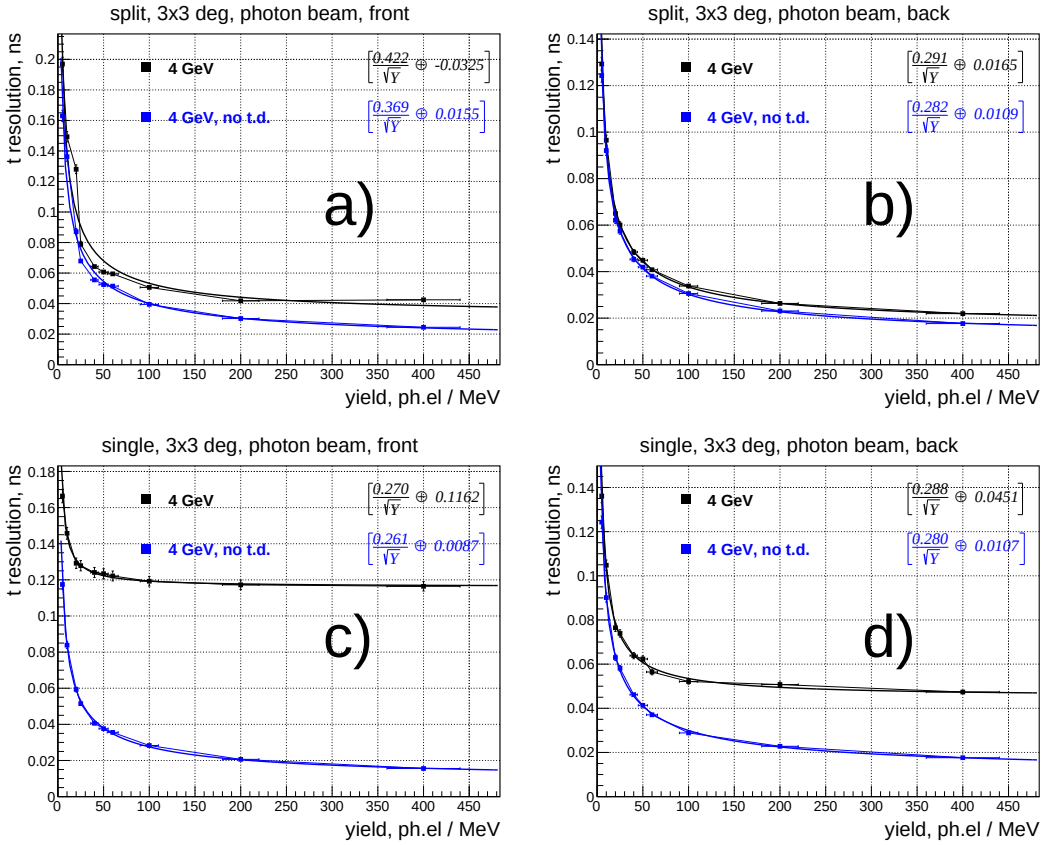


**Figure 11** The values of time resolution for the front and back photodetectors of the split SPACAL module (**a**, **b**) and of the single 14 cm long SPACAL module with continuous fibers (**c**, **d**), as a function of the photoelectron yield. The photon beam energy was 4 GeV. The graphs labeled "no t.d." correspond to the time resolution obtained without taking into account shower development and photon transport, see text.

To study the contribution of shower development and photon transport, we have artificially set the time of photon emission and propagation to zero, leaving only scintillation kinetics and PMT transit time. The time resolution graphs obtained in this assumption are shown at the plots with label "no t.d.".

Figure 8 shows the values of time resolution for the front and back photodetectors of the split (a, b) and continuous (c, d) SPACAL modules, as a function of the photoelectron yield, for the electron beam energy 4 GeV.

From Figures 7 - 8, we can conclude that the time resolution is mainly determined by two factors: number of photoelectrons (which depends on the beam energy and photoelectron yield) and shower fluctuations. However the effect of shower fluctuations is much more pronounced in case of the SPACAL module with continuous fibers, and significantly suppressed in case of the split SPACAL module.

The effect of the shower longitudinal fluctuations can also be seen as correlation between $t_{FRONT}$ and $t_{BACK}$ for the continuous SPACAL module (Figure 9a). This correlation is not observed in case of the split SPACAL (Figure 9b). It confirms that the split SPACAL layout reduces the contribution of shower fluctuations.

Of course, due to this correlation, in the case of SPACAL module with continuous fibers, one can restore the time resolution using linear combination of the time measurements with front and back photodetectors, $t = w \cdot t_{FRONT} + (1 - w) \cdot t_{BACK}$. For example, for the photoelectron yield of 50 per MeV, by using such combination with $w$=0.32, one can obtain the time resolution of 32.4 ps for 4 GeV electrons and 19.8 ps for 10 GeV electrons.

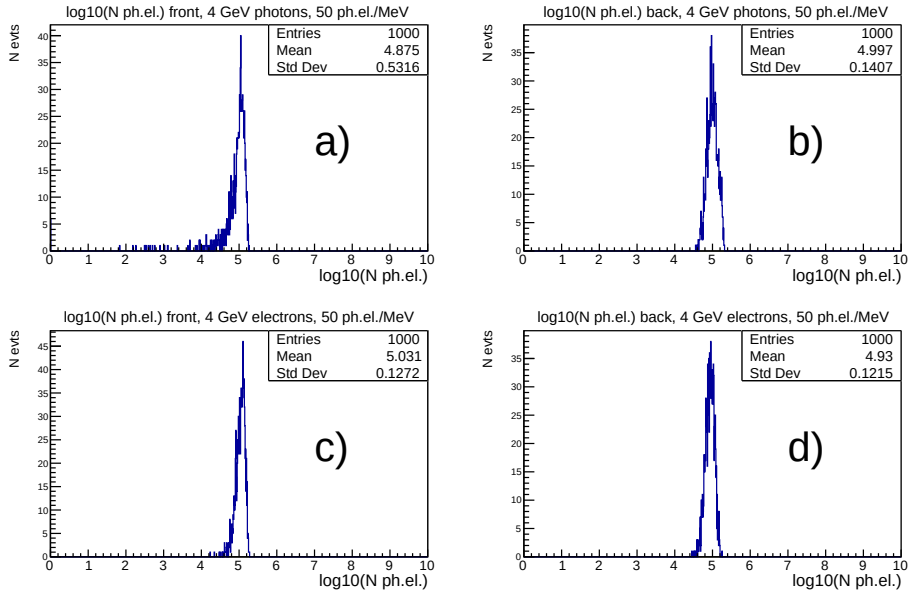


**Figure 12** Distributions of the number of photoelectrons for the incident photon (**a** and **b**) and electron (**c** and **d**) for the front (**a** and **c**) and back (**b** and **d**) photodetectors of the split SPACAL module.

## 5.2 Photon beam

Similar studies of the time resolution were performed for photon beam. Figure 10 shows the values of time resolution for the front and back photodetectors of the split (a, b) and continuous (c, d) SPACAL modules as a function of the incident photon energy, for photoelectron yields of 25 and 50 per MeV.

Figure 11 shows the values of time resolution for the front and back photodetectors of the split (a, b) and continuous (c, d) SPACAL modules, as a function of the photoelectron yield, for the photon beam energy 4 GeV.

The time resolution in the front section of the split SPACAL module for the photon beam is noticeably worse than for the electron beam (Figures 7a, 8a). This can be explained by larger fluctuations in the coordinate of the shower starting point, originating from larger mean free path of high energy photon than that of electron. This leads to higher fluctuations of the energy deposition in the front section, as can be seen in Figure 12. The time resolution of the front photodetector of the single SPACAL module with continuous fibers for the photon beam is also worse than for the electron beam, however to a lesser extent (Figures 7c, 8c).

The dependence of the combined time resolution of the single SPACAL module on beam energy and photoelectron yield for both electron and photon beams is shown in Figure 13. Note that the combined time resolutions for electron and photon beams are very close to each other.

# 6 Concluding remarks

In this work, we have performed a simulation study of time resolution which can be obtained for two versions of SPACAL-like calorimeter modules, namely the longitudinally split module (4 cm + 10 cm) and the single 14 cm long section read out from two sides. The crystal fibers made of GAGG:Ce were used as scintillation elements. Both electrons and photons with energies 1-10 GeV were used as incoming beam.

An analytical approach to the transport of optical photons has been developed. It allows to speed up the calculations, with respect to the full straightforward GEANT4 simulation, by two orders of magnitude.

At the output of the simulation, we generate output pulses of the photodetectors. These pulses are built out of single photoelectron pulses, generated according to the photodetector properties, at a time determined by the arrival time of corresponding optical photon.

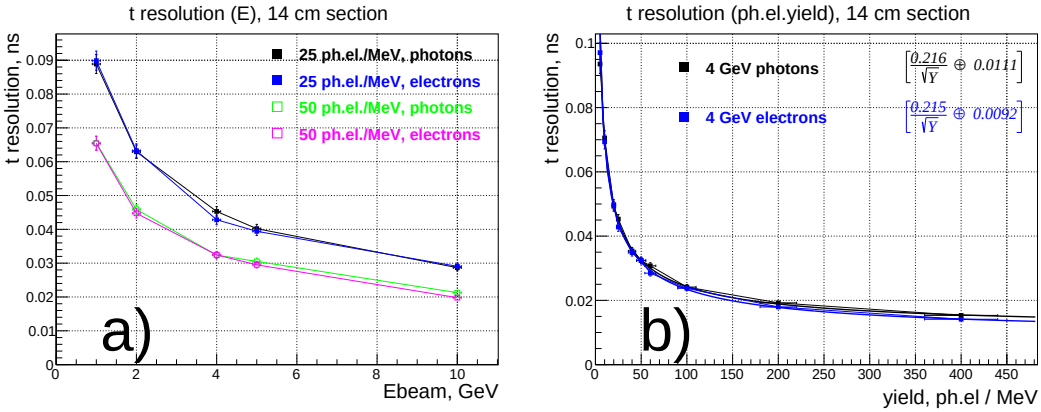


**Figure 13** The energy **a** and photoelectron yield **b** dependence of resolution of combined time measurement, $t = w \cdot t_{FRONT} + (1 - w) \cdot t_{BACK}$, with $w$=0.32.

The next step would be to improve the optical photons transport function, taking into account imperfections of the crystal surfaces.

The main observations are:

- the time resolution improves with increasing the energy of incoming particle, as well as the photoelectron yield of the module;
- in case of single SPACAL module read out from both sides, the contribution of the shower longitudinal fluctuations to the time resolution is quite substantial.
  - However the time resolution can be restored, due to the correlation of the time measurements with the front and back photodetectors.
- On the other hand, using the longitudinally split layout significantly reduces the effect of shower fluctuations;
- we can expect the time resolution of few tens of picoseconds for 5-10 GeV electrons in the split SPACAL module;
  - It can be of the order of 10-20 ps in case of high photoelectron yield, which is in principle achievable by using high quality photodetector and direct optical contact of scintillation fibers and photodetector.
- for the photon beam, the time resolution in the front 4 cm long section of the split SPACAL module is noticeably worse than for the electron beam. The time resolution in the back section is similar to that for the electron beam.

Within this approach, we will be able to study the calorimeter module performance with different signal processing and reconstruction algorithms, as function of a variety of system parameters, for example scintillation kinetics, photodetector properties, properties of the readout electronics, background rate. By varying the scintillation kinetics parameters, the results obtained here can be expanded to a whole family of garnet materials similar to GAGG, including GFAG [9] and crystals with a small fraction of gadolinium substituted with yttrium [10] or lutetium [11] in the crystal matrices.

# 7 References

[1] The LHCb Collaboration 2017 Expression of Interest for a Phase-II LHCb Upgrade: Opportunities in flavour physics, and beyond, in the HL-LHC era, CERN-LHCC-2017-003

[2] M. Lucchini *et al* 2016 IEEE Transactions on Nuclear Science (vol 63 no 2) 10 1109

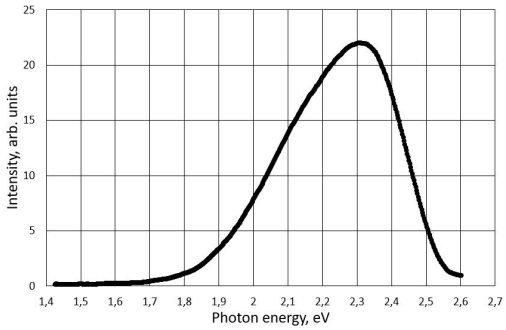


**Figure 14** Typical GAGG luminescence spectrum.

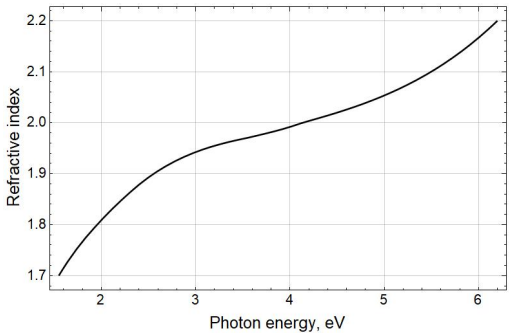


**Figure 15** Typical spectral dependence of GAGG refractive index.

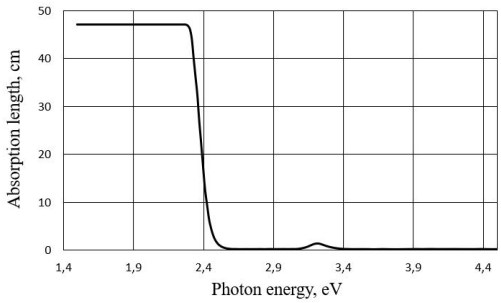


**Figure 16** Spectral dependence of absorption length in GAGG crystal doped with Ce.

[3] V. Alenkov *et al* 2019 Nucl. Instr. and Methods in Phys. Research A 10 1016

[4] GEANT4: http://geant4.cern.ch/

[5] SLITRANI: https://crystalclear.web.cern.ch/crystalclear/LitraniX/Litrani/litrani/index.html

[6] M. Born and E. Wolf, Principles of Optics, 1970

[7] J.D. Jackson, Classical Electrodynamics, J. Wiley & Sons Inc., New York, 1975

[8] Haewook Park *et al*, Achieving reliable coincidence resolving time measurement of PET detectors using multichannel waveform digitizer based on DRS4 chip, 2018 Phys. Med. Biol. 63 24NT02

[9] M.N. Ullah *et al*, Studies on sub-millimeter LYSO:Ce, Ce:GAGG, and a new Ce:GFAG block detector for PET using digital silicon photomultiplier, NIMA 911 (2018) 115-122

[10] Chewpraditkul Weerapong, Scintillation Characteristics of $Mg_2^+$-codoped $Y_{0.8}Gd_{2.2}Al_2Ga_3O_{12}$:Ce Single Crystal, Presented at SCINT2019, 29 September – 4 October 2019, Sendai, Japan

[11] Chewpraditkul Warut, Luminescence and Scintillation Properties of $Mg_2^+$-codoped $Lu_{0.6}Gd_{2.4}Al_2Ga_3O_{12}$:Ce Single Crystal, Presented at SCINT2019, 30 September – 4 October 2019, Sendai, Japan

# 8 Appendix

The characteristics of GAGG crystal used for this study are summarized in Figures 14, 15, 16 and in Table 1.

**Table 1** Parameters of GAGG crystals ($\tau_r$ is the rise time, $\tau_d$ – decay time, $Y$ – light yield, $\rho$ – density)

| | $\tau_r, ps$ | $A$ | $\tau_{d_1}, ns$ | $\tau_{d_2}, ns$ | $Y$, $\frac{ph}{keV}$ | $\rho$, $\frac{g}{cm^3}$ |
|---|---|---|---|---|---|---|
| GAGG | 150 | 0.75 | 70 | 250 | 46 | 6.67 |